

Tsunami run-up and draw-down on a plane beach

By **GEORGE F. CARRIER^{1†}**, **TAI TEI WU¹**
AND **HARRY YEH²**

¹Division of Engineering and Applied Science, Harvard University, USA

²Department of Civil and Environmental Engineering, Box 352700, University of Washington,
Seattle, WA 98195-2700, USA
harryeh@u.washington.edu

(Received 25 March 2002 and in revised form 5 August 2002)

Tsunami run-up and draw-down motions on a uniformly sloping beach are evaluated based on fully nonlinear shallow-water wave theory. The nonlinear equations of mass conservation and linear momentum are first transformed to a single linear hyperbolic equation. To solve the problem with arbitrary initial conditions, we apply the Fourier–Bessel transform, and inversion of the transform leads to the Green function representation. The solutions in the physical time and space domains are then obtained by numerical integration. With this semi-analytic solution technique, several examples of tsunami run-up and draw-down motions are presented. In particular, detailed shoreline motion, velocity field, and inundation depth on the shore are closely examined. It was found that the maximum flow velocity occurs at the moving shoreline and the maximum momentum flux occurs in the vicinity of the extreme draw-down location. The direction of both the maximum flow velocity and the maximum momentum flux depend on the initial waveform: it is in the inshore direction when the initial waveform is predominantly depression and in the offshore direction when the initial waves have a dominant elevation characteristic.

1. Introduction

In 1958, Carrier & Greenspan derived the exact analytical solution of fully nonlinear non-breaking shallow-water waves on a uniformly sloping beach. Because the derivation involves nonlinear and hodograph-type transformations, the Carrier–Greenspan solution is not in a convenient form to be converted to presentations in real time and space domains. For this reason, only a limited number of the practical applications have been reported. Carrier & Greenspan (1958) provided the solution for a monochromatic incident wavetrain, as well as two examples for very specific initial-valued conditions. Spielvogel (1975) applied the Carrier–Greenspan solution to the inverse problem, namely, calculating the incident waveform offshore assuming the initial condition to be a stationary maximum run-up with an exponential profile. Pelinovsky & Mazova (1992) analysed the shoreline trajectories for the incident wave of a Lorenz form. Synolakis (1987) solved the run-up of a wave with a solitary-wave profile over a constant-depth region offshore which then climbed up a uniformly sloped beach. Tadepalli & Synolakis (1994) extended Synolakis's solution to both leading-depression and leading-elevation N-waves. It is noted that both Synolakis

† George Carrier died just prior to the submission of this paper on 8 March 2002.

(1987) and Tadeipalli & Synolakis (1994) had to make significant efforts to solve their specific problems, although they solved the same basic problem but with different initial waveforms. Because of the complexity, their analyses were limited to the determination of the maximum run-up heights and to the analyses of evolution in water-surface profiles. The flow velocity field and the associated shoreline motions were not discussed in depth. More importantly, their solutions are restricted to cases with infinitesimal amplitudes and velocities at the offshore boundary. What we wish to present in this paper is a comprehensive methodology for the accurate run-up/run-down computations for fully nonlinear shallow-water waves throughout the domain. The solutions are conveniently presented in the physical time and space domain. To achieve this, the Green function representation of the solution is first obtained, then numerical integration is performed to express the results in the useful physical forms in real space and time.

2. Analysis

The fully nonlinear shallow-water-wave equations for propagation over a plane beach with a uniform slope α can be written as

$$\begin{aligned} [u'(\alpha x' + \eta')]_{x'} + \eta'_{t'} &= 0, \\ u'_{t'} + u'u'_{x'} + g\eta'_{x'} &= 0, \end{aligned} \quad (1)$$

where u' is the horizontal flow velocity that is assumed uniform over the depth, η' is the vertical departure of the water surface from its quiescent position, g is acceleration due to gravity, x' is the horizontal coordinate pointing offshore from the shoreline of the quiescent state, and t' is time. Note that the primed quantities are dimensional, and the letter subscript represents partial differentiation. The geometry of the problem is depicted in figure 1. The following scaling parameters are introduced:

$$u' = \sqrt{g\alpha L}u, \quad \eta' = \alpha L\eta, \quad x' = Lx, \quad t' = \sqrt{\frac{L}{\alpha g}}t, \quad (2)$$

where L is any convenient horizontal length scale, which may be the distance from the shoreline to the middle of the postulated initial wave condition. Using this scaling, the shallow-water-wave equations (1) can be expressed in the following dimensionless forms:

$$\begin{aligned} [u(x + \eta)]_x + \eta_t &= 0, \\ u_t + uu_x + \eta_x &= 0. \end{aligned} \quad (3)$$

Note that the beach slope α and the acceleration due to gravity g no longer appear in these governing equations.

Further transformation of (3) is made by introducing the distorted coordinates q and λ such that

$$\lambda = t - u, \quad q = x + \eta. \quad (4)$$

Note that

$$x_q = 1 - \eta_q, \quad x_\lambda = -\eta_\lambda, \quad t_q = u_q, \quad t_\lambda = 1 + u_\lambda. \quad (5)$$

The Jacobian of the transformation is $J = x_q t_\lambda - x_\lambda t_q$, and unless J (or $1/J$) vanishes somewhere in the (x, t) -domain, the transformation is single-valued. It follows from (5) that

$$q_x = \frac{t_\lambda}{J}, \quad q_t = -\frac{x_\lambda}{J}, \quad \lambda_x = -\frac{t_q}{J}, \quad \lambda_t = \frac{x_q}{J}. \quad (6)$$

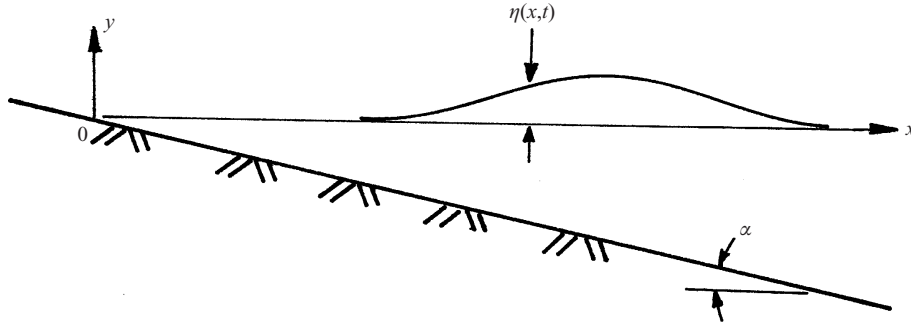


FIGURE 1. A definition sketch.

Then, the transformation of (3) yields

$$\begin{aligned} (qu)_q + \left(\eta + \frac{u^2}{2} \right)_\lambda &= 0, \\ u_\lambda + \left(\eta + \frac{u^2}{2} \right)_q &= 0. \end{aligned} \quad (7)$$

It is convenient to write $\psi = \eta + \frac{1}{2}u^2$, and replace q by σ^2 , such that $\sigma = \sqrt{q} = \sqrt{x + \eta}$. Note that $\sigma = 0$ represents the moving shoreline, and, since $q \geq 0$, σ is always real in the fluid domain. Then, (7) becomes

$$\begin{aligned} (\sigma^2 u)_\sigma + 2\sigma \psi_\lambda &= 0, \\ u_\lambda + \frac{1}{2\sigma} \psi_\sigma &= 0, \end{aligned} \quad (8)$$

and the elimination of u yields

$$4\sigma \psi_{\lambda\lambda} - (\sigma \psi_\sigma)_\sigma = 0 \quad (9)$$

Equation (9) is the same form as that derived by Carrier & Greenspan (1958), but with slightly different non-dimensionalization.

We can also write

$$\psi = \eta + \frac{1}{2}u^2 = \varphi_\lambda, \quad u = -\frac{\varphi_\sigma}{2\sigma}, \quad \eta = \varphi_\lambda - \frac{\varphi_\sigma^2}{8\sigma^2}. \quad (10)$$

It is evident that the potential φ also satisfies (9):

$$4\sigma \varphi_{\lambda\lambda} - (\sigma \varphi_\sigma)_\sigma = 0. \quad (11)$$

Equation (11) is a second-order partial differential equation, which requires two independent initial conditions at $\lambda = 0$ to solve for a unique solution. Synolakis (1987) and Tadepalli & Synolakis (1994) imposed a single initial condition in terms of ψ , approximating $\psi \approx \eta$ in their problems. The other necessary initial condition, ψ_λ , was implicitly incorporated in their solution form, restricting their initial condition to steady propagation of the incident linear wave offshore.

Without such restrictions, we consider the general initial conditions:

$$\varphi(\sigma, 0) = P(\sigma), \quad \varphi_\lambda(\sigma, 0) = F(\sigma), \quad (12)$$

in which

$$P(\sigma) = - \int_0^\sigma 2\sigma' u(\sigma', 0) d\sigma', \quad F(\sigma) = \eta(\sigma, 0) + \frac{1}{2}u^2(\sigma, 0). \quad (13)$$

To solve this problem, we use the Fourier–Bessel transform (also called the Hankel transform) of the form

$$\bar{\varphi}(\rho, \lambda) = \int_0^\infty \sigma J_0(\rho\sigma) \varphi(\sigma, \lambda) d\sigma, \quad (14)$$

in which the inversion identity is

$$\varphi(\sigma, \lambda) = \int_0^\infty \rho J_0(\rho\sigma) \bar{\varphi}(\rho, \lambda) d\rho. \quad (15)$$

Note that the transformed initial conditions are expressed as

$$\bar{\varphi}(\rho, 0) = \bar{P}(\rho), \quad \bar{\varphi}_\lambda(\rho, 0) = \bar{F}(\rho). \quad (16)$$

Multiplying (11) by $J_0(\rho\sigma)$ and integrating each side of that equation from zero to ∞ , using integration by parts, yields

$$\bar{\varphi}_{\lambda\lambda} + \frac{1}{4}\rho^2\bar{\varphi} = 0, \quad (17)$$

whose solution, using (16), is

$$\bar{\varphi}(\rho, \lambda) = \bar{P}(\rho) \cos(\rho\lambda/2) + \frac{2}{\rho} \bar{F}(\rho) \sin(\rho\lambda/2). \quad (18)$$

Inversion of (18) using (15) can be obtained as

$$\begin{aligned} \varphi(\sigma, \lambda) &= \int_0^\infty \rho J_0(\rho\sigma) \{ \bar{\varphi}(\rho, 0) \cos \rho\lambda/2 + (2/\rho) \bar{\varphi}_\lambda(\rho, 0) \sin \rho\lambda/2 \} d\rho \\ &= 2 \frac{\partial}{\partial \lambda} \int_0^\infty P(\sigma'') \left[\sigma'' \int_0^\infty J_0(\rho\sigma) \sin(\rho\lambda/2) J_0(\rho\sigma'') d\rho \right] d\sigma'' \\ &\quad + 2 \int_0^\infty F(\sigma'') \left[\sigma'' \int_0^\infty J_0(\rho\sigma) \sin(\rho\lambda/2) J_0(\rho\sigma'') d\rho \right] d\sigma''. \end{aligned} \quad (19)$$

The derivation of (19) is presented in Appendix A. Equation (19) can be rewritten in a Green function presentation as

$$\varphi(\sigma, \lambda) = 2 \left\{ \int_0^\infty F(b) G(b, \sigma, \lambda) db + \int_0^\infty P(b) G_\lambda(b, \sigma, \lambda) db \right\}, \quad (20)$$

where

$$G(b, \sigma, \lambda) = b \int_0^\infty J_0(\rho\sigma) \sin(\rho\lambda/2) J_0(\rho b) d\rho \quad (21)$$

is the Green function which would permit the determination of the $\varphi(\sigma, \lambda)$ that would ensue from the initial condition (12). The Green function (21) can be explicitly evaluated as

$G(b, \sigma, \lambda) =$

$$\begin{cases} 0 & \text{for } \frac{1}{2}\lambda < |\sigma - b| \\ \frac{1}{\pi} \sqrt{\frac{b}{\sigma}} K\left(\frac{\lambda^2 - 4(\sigma - b)^2}{16\sigma b}\right) & \text{for } |\sigma - b| < \frac{1}{2}\lambda < |\sigma + b| \\ \frac{4}{\pi} \frac{b}{\sqrt{\lambda^2 - 4(\sigma - b)^2}} K\left(\frac{16\sigma b}{\lambda^2 - 4(\sigma - b)^2}\right) & \text{for } \frac{1}{2}\lambda > |\sigma + b| \end{cases} \quad (22)$$

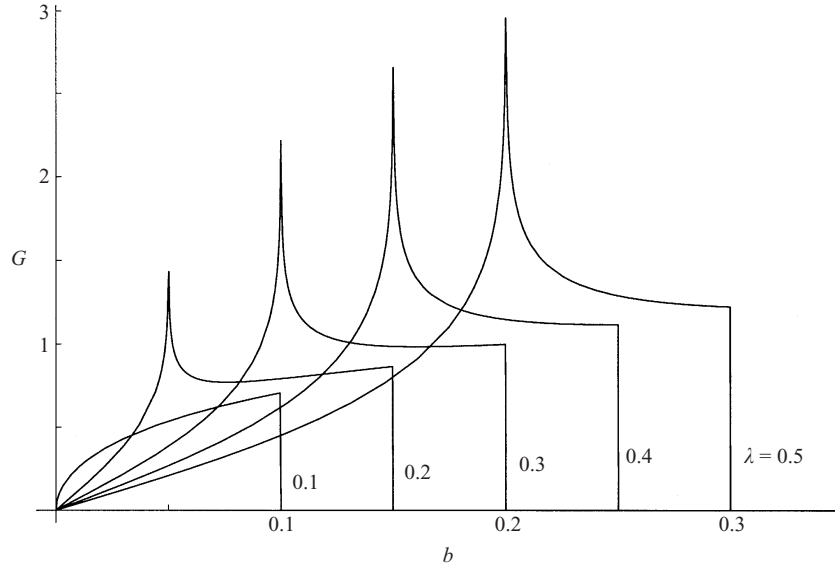


FIGURE 2. The Green function $G(b, \sigma, \lambda)$ for $\lambda = 0.1, 0.2, 0.3, 0.4$ and 0.5 with $\sigma = 0.05$.

where $K(k) = \int_0^{\pi/2} dv / \sqrt{1 - k \sin^2 v}$ is the complete elliptic integral of the first kind. The derivation of (22) is presented in Appendix B. The Green function has a singularity at $b = \frac{1}{2}\lambda - \sigma$ as shown in figure 2, none the less, (20) can be integrated numerically with a standard integration software (e.g. the IMSL library) for any regular initial conditions in (12).

3. Results

We first consider the initial condition with nil velocity everywhere, but the water surface is displaced at $t = 0$. This condition is typically assumed for tsunami generation, because the horizontal scale of the seismic sea-floor dislocation is much larger than the vertical scale, hence the time scale of the dislocation is effectively much shorter than the flow establishment. For the case of $u = 0$, $\lambda = 0$ exactly. Furthermore, $F(\sigma) = \psi(\sigma, 0) = \varphi_\lambda(\sigma, 0) = \eta(\sigma)$ at $\lambda = 0$, without approximation.

As an example, the initial water-surface displacement of Gaussian shape is imposed:

$$\eta = a \exp\{-k(x - x_0)^2\} \approx a \exp\{-k(\sigma^2 - \sigma_0^2)^2\} \quad \text{for } \eta \ll x. \quad (23)$$

Hence, we set

$$F(b) = a \exp\{-k(b^2 - b_0^2)^2\}, \quad P(b) = 0. \quad (24)$$

The initial wave with $a = 0.017$, $b_0 = 1.3$ ($x_0 = 1.69$) and $k = 4.0$ is shown in figure 3. Note that the approximation made in (23) is simply for convenience, which results in the initial water-surface displacement slightly deviated from the exact Gaussian shape; full nonlinearity is still retained in our solution, however. Equation (20) is integrated using the IMSL library, and the result $\varphi(\sigma, \lambda)$ is plotted in figure 4. The physical (yet non-dimensionalized) variables in the (x, t) -space are computed using (10) and then (4). Figures 5 and 6 show the temporal and spatial variations of water-surface displacement η and water velocity u , respectively. The excursion of the shoreline is small ($-0.047 < x < 0.017$) for the scale of the figures, and is not presented. (The shoreline locations will be presented explicitly later when we discuss

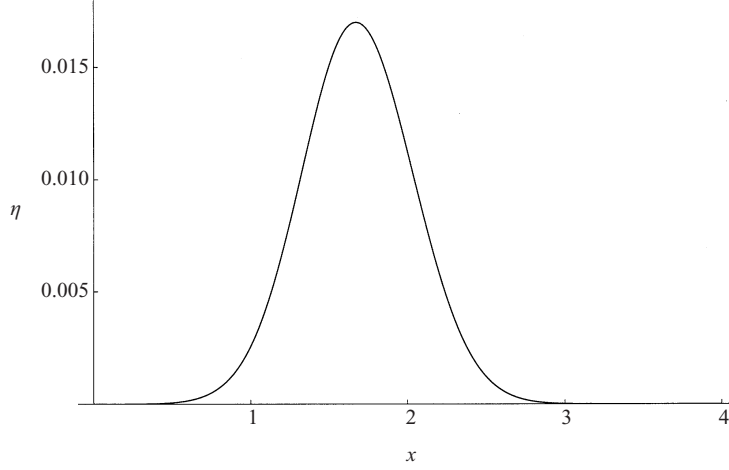


FIGURE 3. The initial waveform of a Gaussian shape (23) with $a = 0.017$, $b_0 = 1.3$ and $k = 4.0$. The flow velocity is nil everywhere.

the run-up and draw-down motions.) Figures 5 and 6 show that the initial static water-surface displacement evolves into the incoming, outgoing and reflected waves. Figure 7 shows the snapshots of wave profile at $t = 1.0$, that is extracted from figure 5, and the wave profile at $t = 5.3$. The profile at $t = 5.3$ (figure 7b) is obtained by computing only in the narrow range of λ (i.e. $5.25 < \lambda < 5.35$); our method can obtain the solution for arbitrarily selected time and location without computing the rest of the computational domain. Figure 7(a) shows the incoming wave and the outgoing wave generated from the initial static water-surface deformation. The incident wave of single elevation causes the reflected wave in the dipole formation (figure 7b) as demonstrated earlier by Carrier & Noiseux (1983).

The next example is to set the initial condition to be an incident wave from offshore, i.e. $u(x, t = 0) \neq 0$. The initial velocity field is approximated by neglecting nonlinear effects. This is justified by the fact that the wave is essentially linear far offshore: $\frac{1}{2}u^2 \ll O(1)$ and $\eta u_x \ll O(1)$. Hence, we approximate the velocity field by

$$u \approx \frac{\eta}{\sqrt{x}}. \quad (25)$$

For the Gaussian shaped initial wave in the form (23), we set

$$F(b) = a \exp\{-k(b^2 - b_0^2)^2\},$$

and

$$P(b) = - \int_0^b 2\eta(b', 0) db' = - \int_0^b 2a \exp\{-k(b'^2 - b_0^2)^2\} db'. \quad (26)$$

The difficulty arises from the computation of the term

$$\int_0^\infty P(b) G_\lambda(b, \sigma, \lambda) db \left(= \frac{\partial}{\partial \lambda} \int_0^\infty P(b) G(b, \sigma, \lambda) db \right) \quad (27)$$

in (20) which contains the highly singular function $G_\lambda(b, \sigma, \lambda)$, especially for small σ . A satisfactory computation can be made for a small value of the initial amplitude, a . Figure 8 shows the water-surface displacement η in the (x, t) -space with the initial wave parameters: $a = 0.0025$, $b_0 = 1.3$ and $k = 4.0$. Figure 9 shows the spatial profiles

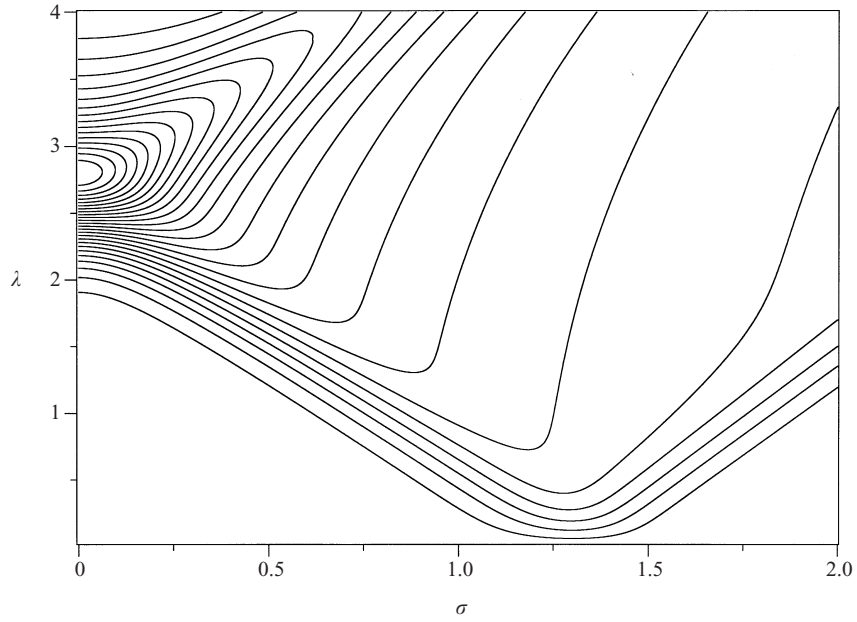


FIGURE 4. $\varphi(\sigma, \lambda)$ computed by (20) for the initial Gaussian shaped water-surface displacement defined in (23) with $a = 0.017$, $b_0 = 1.3$ and $k = 4.0$.

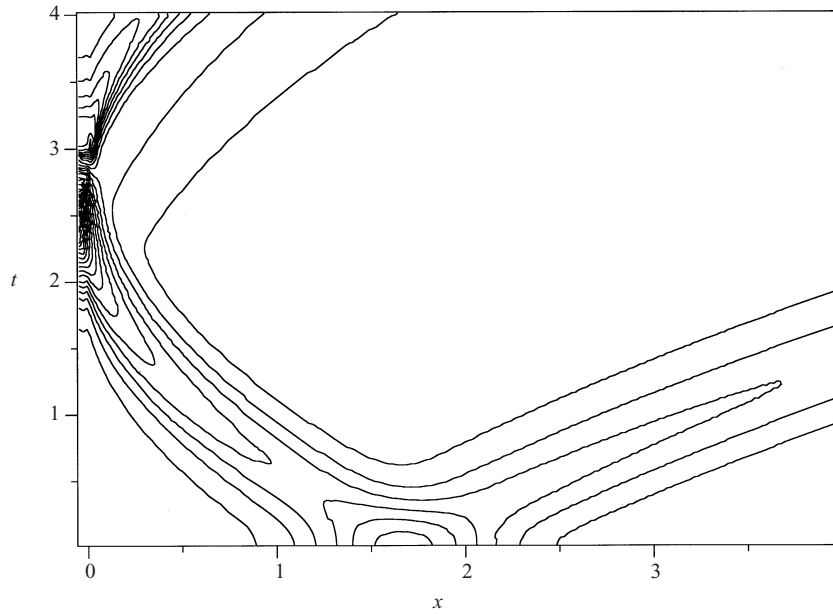


FIGURE 5. Water-surface trajectory corresponding to $\varphi(\sigma, \lambda)$ shown in figure 4 for the initial Gaussian shaped water-surface displacement defined in (23) with $a = 0.017$, $b_0 = 1.3$ and $k = 4.0$.

of water surface at $t = 1.0$ that are extracted from figure 8. In contrast to the plots shown in figures 5 and 7(a), figures 8 and 9 clearly exhibit no outgoing wave from the initial wave location; there is minute outgoing-wave noise, owing perhaps to the mismatch caused by the linear approximation for u , although it is too small to appear in figures 8 and 9.

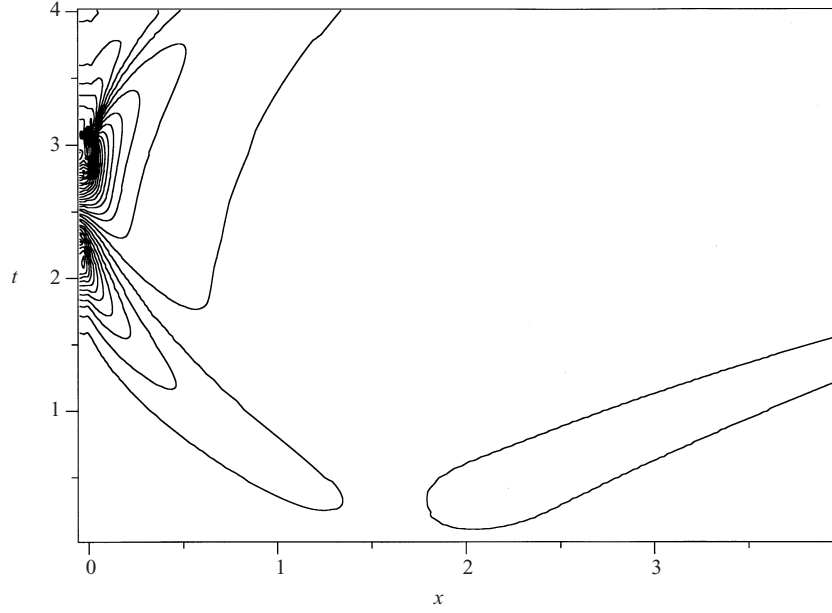


FIGURE 6. Flow velocity trajectory corresponding to $\varphi(\sigma, \lambda)$ shown in figure 4 for the initial Gaussian shaped water-surface displacement defined in (23) with $a = 0.017$, $b_0 = 1.3$ and $k = 4.0$.

4. Applications

With the solution procedure described, we now examine the detailed run-up and run-down motions. Such information is useful to analyse in preparation for a tsunami attack on the shore. The following four cases of the initial static water-surface deformation are examined:

(a) The Gaussian shape as described in (23).

(b) The negative Gaussian shape, that is the inverse profile of case a:

$$\eta = -a \exp\{-k(x - x_0)^2\} \quad \text{with} \quad \{a = 0.017, k = 4.0, x_0 = 1.69\}. \quad (28)$$

(c) The leading depression N-wave shape, typically caused by a seismic fault dislocation by subduction earthquake

$$\eta = a_1 \exp\{-k_1(x - x_1)^2\} - a_2 \exp\{-k_2(x - x_2)^2\}$$

with $\{a_1 = 0.02, a_2 = 0.01, k_1 = k_2 = 3.5, x_1 = 1.5625, x_2 = 1.0\}$. (29)

(d) The leading depression N-wave shape, typically caused by an offshore submarine landslide:

$$\eta = a_1 \exp\{-k_1(x - x_1)^2\} - a_2 \exp\{-k_2(x - x_2)^2\}$$

with $\{a_1 = \frac{1}{3}a_2 = 0.006, a_2 = 0.018,$

$$k_1 = \frac{1}{9}k_2 = 0.4444, k_2 = 4.0, x_1 = 4.1209, x_2 = 1.6384\}. \quad (30)$$

Recall that our problem in the non-dimensional form of (3) is independent of the beach slope. The constants used in the above examples are selected so that the initial waveform for each case has approximately the same maximum amplitude as well as the breadth of the primary displacement. Table 1 contains the details of the values of the maximum initial displacements. The initial waveforms are shown in figure 10.

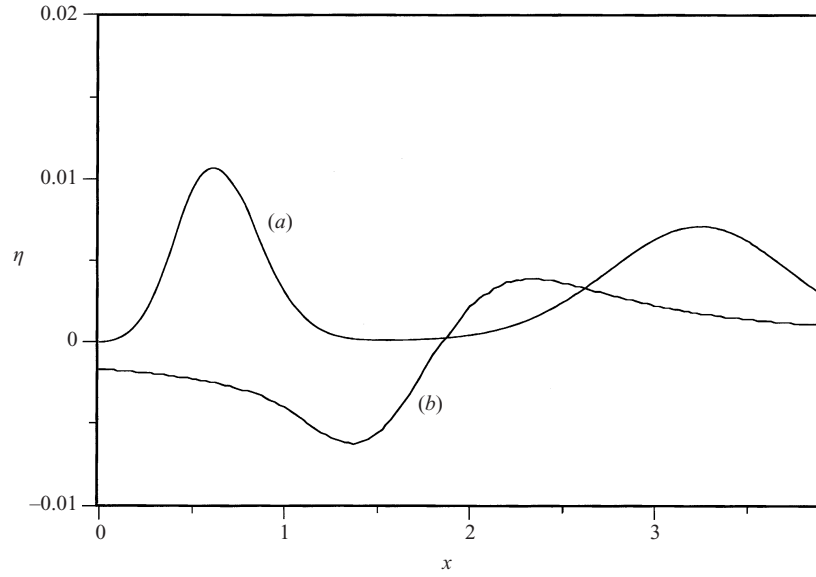


FIGURE 7. The water-surface profile evolved from the initial Gaussian-shaped displacement of figure 3. (a) Incident and outgoing waves at $t = 1.0$ extracted from figure 5. (b) Reflected wave at $t = 5.3$.

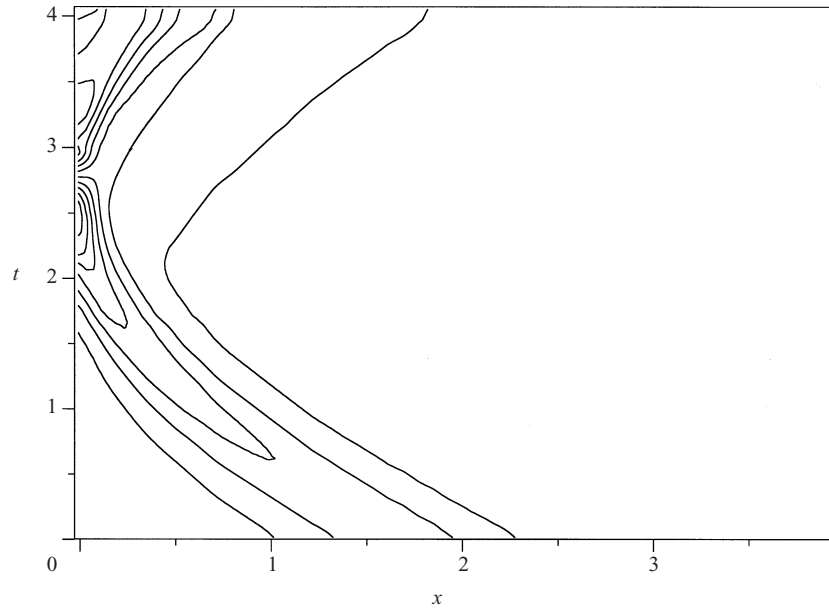


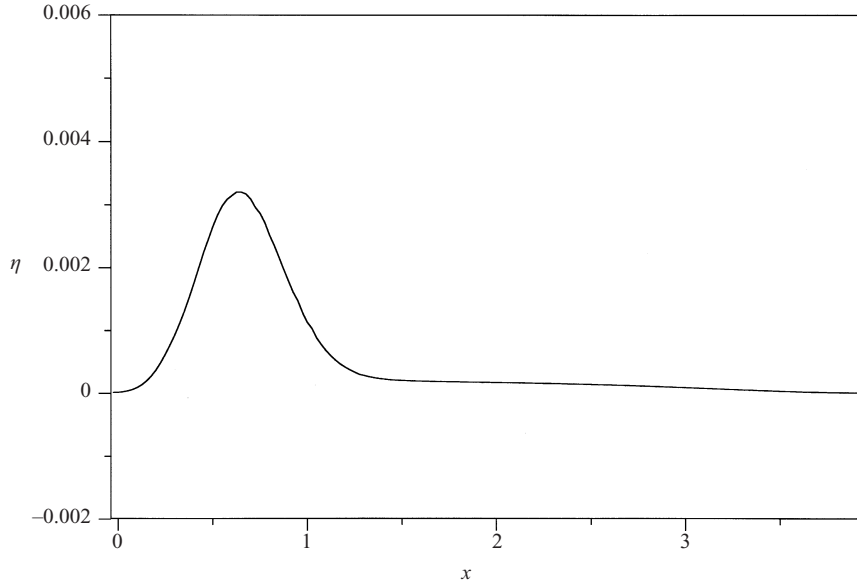
FIGURE 8. Water-surface trajectory for the initial Gaussian-shaped incident wave defined in (26) with $a = 0.0025$, $b_0 = 1.3$ and $k = 4.0$.

Note that the parameters used in case d—the initial wave caused by a submarine landslide—keep the displaced water mass conserved, i.e. the integrated amount of the positive dislocation is identical to that of the negatively dislocated volume.

All of the constant parameters are non-dimensional quantities. Considering the centroid of initial displacement at 75 km offshore with the beach slope of $\frac{1}{200}$, then the

	Case a	Case b	Case c	Case d
Initial maximum displacement	0.0170	-0.0170	0.0173	-0.0175
Maximum run-up	-0.0470	-0.0268	-0.0583	-0.0328
Maximum draw-down	0.0268	0.0470	0.0235	0.0484
Maximum shoreward velocity	-0.103	-0.213	-0.1634	-0.225
	at $x = -0.0260$	at $x = 0.0333$	at $x = -0.0167$	at $x = 0.0348$
Maximum offshore velocity	0.213	0.103	0.226	0.104
	at $x = 0.0122$	at $x = 0.0365$	at $x = 0.00666$	at $x = 0.0370$
Maximum momentum flux	0.000471	-0.000471	0.000576	-0.000567
	at $x = 0.0287$	at $x = 0.0479$	at $x = 0.0254$	at $x = 0.0493$

TABLE 1. Some extreme values of the results.

FIGURE 9. The water-surface profile at $t = 0$ evolved from the initial Gaussian-shaped incident wave extracted from figure 8.

horizontal length scale parameter L in (2) can be set to 75 km. In case a (Gaussian initial wave), the constant $a = 0.017$ represents the maximum water-surface amplitude of approximately 6 m; this amplitude represents a significant but realistic tsunami source. For case d (wave generated by the submarine landslide), if the submarine landslide is generated at 5 km offshore with the beach slope of $\frac{1}{10}$, then the maximum water-surface depression would be approximately 9 m, which also reflects a realistic event. In other words, all four models represent very realistic tsunami initial conditions.

Figures 11 and 12 show the temporal and spatial variations of the water-surface elevation and the inundation depth, respectively, for the four cases. Temporal variations of the shoreline locations are also shown. The computations are made only for the run-up and run-down regions near the shore, i.e. $1.5 < t < 3.5$ and $x < 0.15$; the computations were not made in the offshore region and $t < 1.5$. Unlike ordinary numerical simulation models, the computational domain in x and t can be selective, taking the advantage of our analytical-numerical hybrid model.

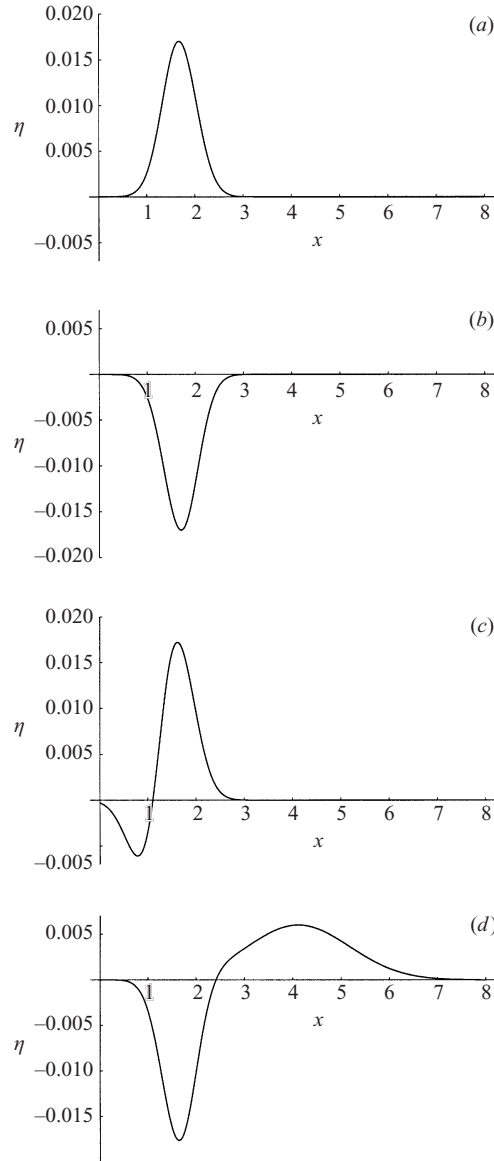


FIGURE 10. Initial waveforms. (a) Gaussian shape, (b) negative Gaussian shape, (c) leading N-wave caused by fault dislocation, (d) leading N-wave caused by submarine landslide.

Temporal variations of the shoreline locations shown in figures 11 and 12 show that the initial waveforms of the predominantly positive displacement, cases a and c, result in higher run-up heights than the heights caused by the initial waveforms of the predominantly negative displacement, cases b and d. The converse can be observed for the withdrawal distances; those in cases b and d are greater than cases a and c.

In spite of their equal positive displacements in cases a and c, the maximum run-up height is substantially greater in case c (the leading depression N-wave) than in case a (the single positive displacement of the Gaussian shape): the max $|x| = 0.0470$ for case a and 0.0583 for case c, as shown in table 1. This higher run-up height of the leading depression N-wave is consistent with the findings of Mazova & Pelinovsky (1991) and

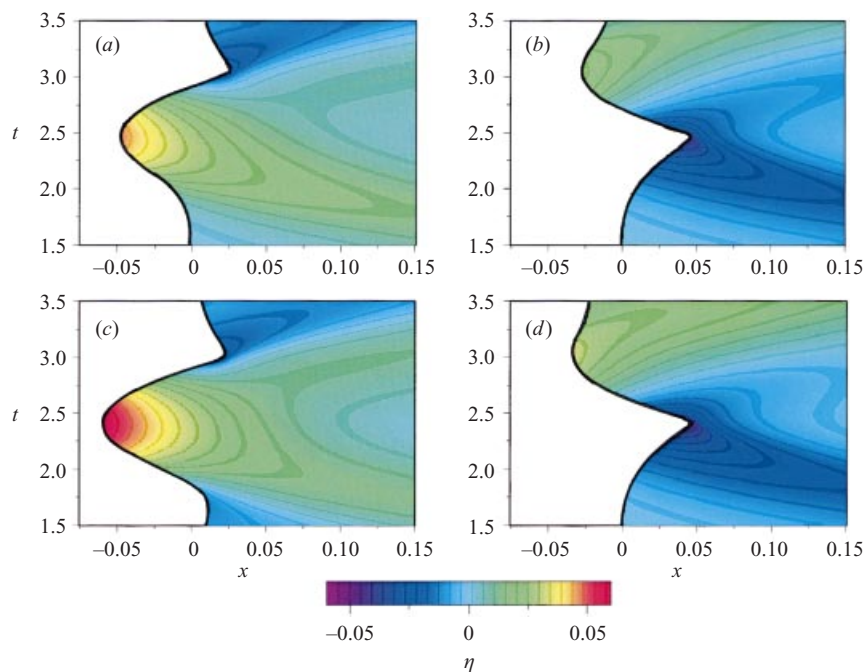


FIGURE 11. Temporal and spatial variations of the water-surface elevation for (a) the initial waveform is the Gaussian shape (case a), (b) the negative Gaussian shape (case b), (c) the leading depression N-wave (case c), and (d) the waveform caused by the submarine landslide (case d).

Tadepalli & Synolakis (1994). The wave reflection pattern shown in figure 12 indicates that the reflection of the small negative leading wave in case c causes a steepening of the subsequent positive wavefront; such an effect is observed by comparing the run-up in cases a and c near $t = 2.0$. The steepening of the wavefront appears to cause a higher run-up height in case c than in case a. On the other hand, the reflection of the large negative leading wave in case d appears to reduce the subsequent positive wave surge.

The magnitude of the maximum run-up height of case a (positive Gaussian wave) is identical to that of the minimum shoreline elevation of case b (negative Gaussian wave), and the maximum run-up height of case b has an equal magnitude to the minimum of case a (see table 1). This coincidence may be interpreted as the extreme shoreline location computed by fully nonlinear theory being identical to those predicted by linear theory, whereas the shoreline trajectories and waveforms are different for the two cases as observed in figures 11 and 12. This characteristic was pointed out by Carrier (1971) and also discussed by Synolakis (1987).

It is also observed in figure 11, as well as in figure 12, that the water-surface contours in case c are approximately symmetrical about the time of maximum run-up, $t = 2.4$, while the contours for other cases are skewed, even for cases a and c in spite of the symmetric initial water-surface displacement. The inversion of initial water-surface displacement in cases a and b does not result in simple replacement of the positive with the negative in their run-up and run-down processes. Clearly, nonlinear effects are important for the run-up/run-down processes. In spite of this nonlinear effect, as we discussed earlier, the maximum inundation height of case a is identical to the minimum draw-down of case b. The maximum inundation depth at $x = 0$ (the

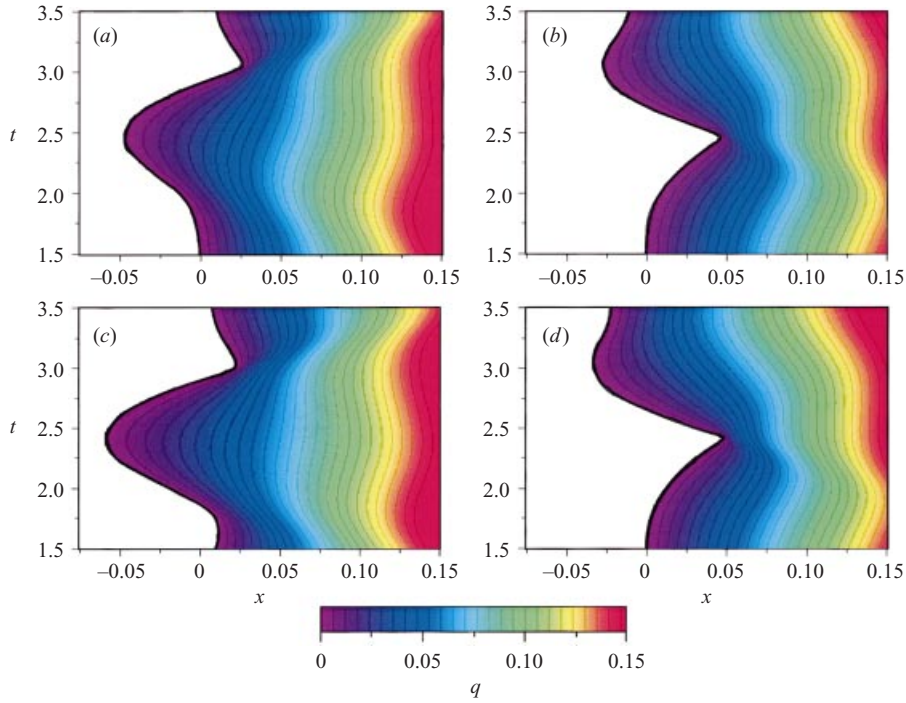


FIGURE 12. Temporal and spatial variations of the inundation depth for (a) the initial waveform is the Gaussian shape (case a), (b) the negative Gaussian shape (case b), (c) the leading depression N-wave (case c), and (d) the waveform caused by the submarine landslide (case d).

shoreline location at the quiescent state) occurs prior to the occurrence of maximum run-up in case a, while it occurs after the maximum run-up in cases b and d, when the primary initial wave is a depression. Case c shows that the maximum inundation depth at $x = 0$ and the maximum shoreline run-up take place at approximately the same time.

Figure 13 shows the flow velocities in the (x, t) -plane. In every case, the maximum and minimum flow velocities occur at the shoreline. The reversal of flow direction is gradual at the maximum penetration of the wave, whereas it is rapid at the extreme draw-down position. It is also evident that the maximum flow velocities occur near the minimum draw-down position.

Temporal variations of the shoreline velocities u_s are shown in figure 14. Note that the positive value in velocity represents the offshore direction. Figure 14 shows that for cases a and c (predominantly positive displacement in the initial waveform), the maximum shoreline speed occurs during the draw-down process, i.e. in the offshore direction. On the other hand, the maximum speed occurs during the run-up process, i.e. in the inshore direction, for cases b and d, which are generated by predominantly negative initial water-surface displacement. This shoreline velocity behaviour implies that objects (e.g. sediments, boulders, etc.) will probably be carried inshore in the event of predominantly negative initial waves, whereas they will be carried offshore in the case of positive initial waves. This subject will be revisited later when we discuss wave forces.

As observed in figure 14, temporal variations of the shoreline velocities in cases a and b do not exhibit mirror images about the level of $u_s = 0$. For example, the rate

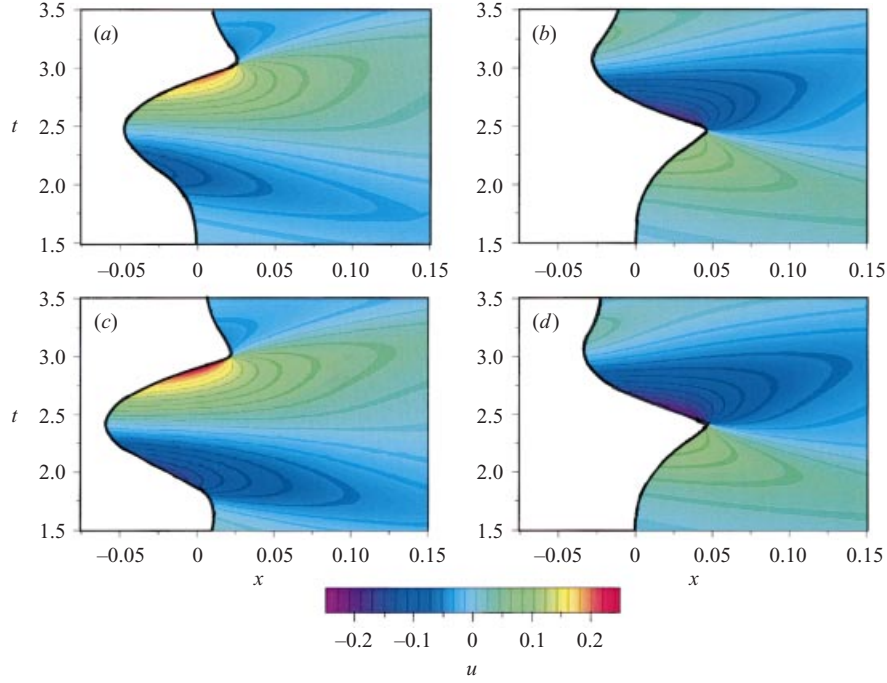


FIGURE 13. Temporal and spatial variations of the fluid velocity for (a) the initial waveform is the Gaussian shape (case a), (b) the negative Gaussian shape (case b), (c) the leading depression N-wave (case c), and (d) the waveform caused by the submarine landslide (case d).

of increase in velocity during the draw-down process in case a is much slower than the rate of increase in run-up velocity in case b. In spite of evidently asymmetric processes in run-up and draw-down of cases a and b, the magnitude of the maximum velocity turns out to be identical, as presented in table 1.

To find the shoreline velocity variations in space, figure 15 contains parametric plots of the shoreline velocity and the shoreline location. The trajectory for case a in the (x, u) -space resembles that for case c, and also case b resembles case d. The extreme velocities in the inshore and offshore directions occur at almost the same offshore location ($x \approx 0.035$) in cases b and d, whereas in cases a and c, the maximum run-up velocity occurs at a slightly inshore location ($x < 0$). However, the maximum draw-down velocity results immediately before the extreme draw-down location. Another observation is that the velocity excursion loop of case a is not the reverse of case b, and they are qualitatively different.

The linear-momentum flux associated with the run-up and run-down is evaluated from the inundation depth and the velocity, i.e. figures 12 and 13, respectively. The momentum flux per unit breadth, based on the approximation of the quasi-steady flows can be expressed as

$$f = qu^2, \quad (31)$$

which can be interpreted as the drag force per unit breadth for a surface-piercing stationary object being placed vertically over the flow depth. Hence, the quantity evaluated by (31) provides a measure for the net force exerted on such an object.

Figure 16 shows the computed momentum-flux fields. For all four cases, the maximum momentum flux occurs near the extreme draw-down location, $x > 0$, and

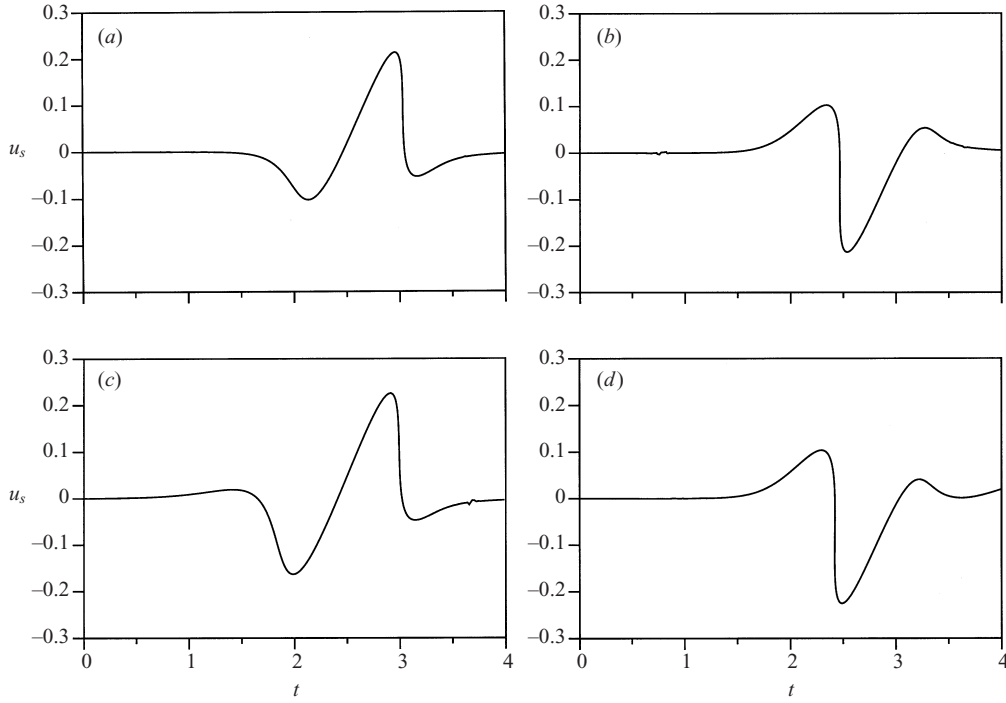


FIGURE 14. Temporal variations of shoreline velocity: (a) the initial waveform is the Gaussian shape (case a), (b) the negative Gaussian shape (case b), (c) the leading depression N-wave (case c), and (d) the waveform caused by the submarine landslide (case d).

immediately prior to, or after, the flow reversal. For predominantly positive initial waves (cases a and c), the maximum momentum flux results during the draw-down phase and points offshore. On the other hand, for the cases of predominantly negative initial waveform (cases b and d), the maximum momentum flux occurs during the run-up immediately after the extreme draw-down, acting in the inshore direction. Also note that for the incident wave of leading depression N-wave (case c), both inshore and offshore forces are significant, although the draw-down force is still greater. The magnitude of the maximum value of f for each case is given in table 1. The maximum momentum flux for the initial Gaussian wave (case a) is identical to that for the negative Gaussian wave (case b), although their directions are opposite. It is noted that the corresponding values of the flow velocity u and the inundation depth q are also identical for the two cases, except the value of u has the opposite sign.

5. Summary and discussion

An improved method is developed to compute tsunami run-up and run-down motions onto a uniformly sloping beach. The method is based on the Green function representation of fully nonlinear shallow-water-wave theory. It is robust and general, for it is capable of computing both incoming and outgoing waves with arbitrary initial wave conditions. Unlike the ordinary time-stepping numerical methods (e.g. finite-difference, finite-element and boundary-element method), the present analytical-numerical hybrid method can analyse for an arbitrarily selected temporal and spatial domain without computing for other domains. Hence, detailed and accurate compu-

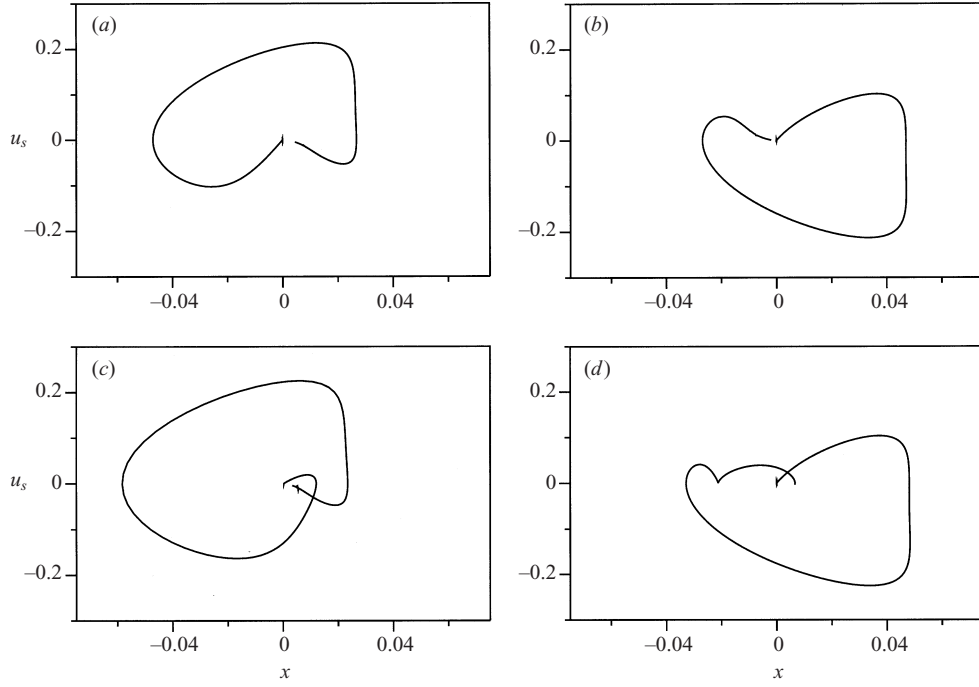


FIGURE 15. Parametric plots of shoreline velocity *vs.* shoreline location: (a) the initial waveform is the Gaussian shape (case a), (b) the negative Gaussian shape (case b), (c) the leading depression N-wave (case c), and (d) the waveform caused by the submarine landslide (case d).

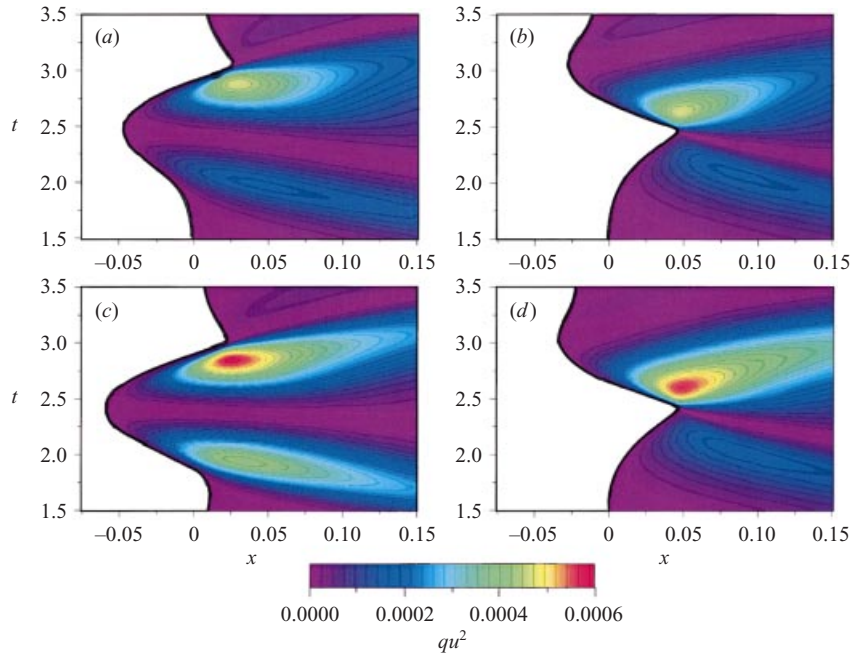


FIGURE 16. Temporal and spatial variations of the linear-momentum flux for (a) the initial waveform is the Gaussian shape (case a), (b) the negative Gaussian shape (case b), (c) the leading depression N-wave (case c), and (d) the waveform caused by the submarine landslide (case d).

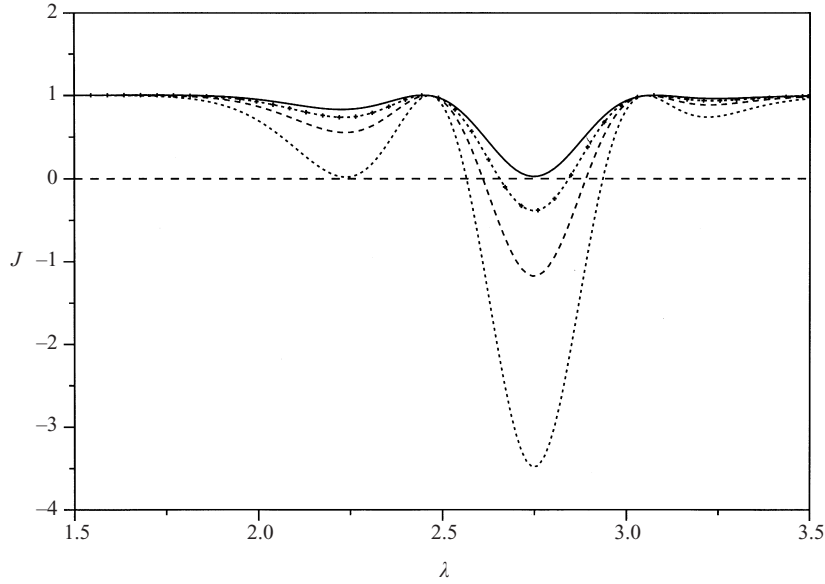


FIGURE 17. The Jacobian of the transformation $J = x_q t_\lambda - x_\lambda t_q$ for case a: —, $\sigma = 0.04$; +, 0.03; ---, 0.02; ----, 0.01.

tations can be made conveniently for a focused domain. It is anticipated that the solutions can be used for validation of traditional numerical codes, especially to test their performance in the prediction of the shoreline movements and the run-up/run-down velocity fields.

Drawbacks of this method include the following: (i) it is only applicable for the problems in one spatial dimension with a uniformly sloping beach, and (ii) once the value of the Jacobian of the transformation, $J = x_q t_\lambda - x_\lambda t_q$, becomes zero, physical interpretations of the solution become uncertain. For example in case a, the Jacobian vanishes a few times, but the occurrence is limited very close to the shoreline $\sigma < 0.04$ as demonstrated in figure 17. As pointed out by Synolakis (1987) with his experimental laboratory results, even if the Jacobian becomes zero at the tip of the shoreline, the solution of nonlinear shallow-water-wave theory recovers immediately and yields extremely accurate predictions for later times.

Using our new method, we examined four initial wave conditions which represent typical tsunami generations: case a, the positive water-surface displacement of Gaussian shape; case b, the negative displacement of Gaussian shape; case c, the leading depression N-wave; and case d, the wave having a water-surface characteristic generated by a submarine-landslide. Cases a and c are predominantly positive initial waves, whereas cases b and d have predominantly negative initial waveforms. It was found that the gross characteristics in the initial waveform are important for the behaviours in run-up and run-down motion, i.e. the motions in cases a and c are similar, and cases b and d are also similar. The following characteristics and behaviours of the run-up and draw-down processes were found in our study:

(i) When the initial waveform is positive (including case c, the leading depression N-wave), the run-up elevation is greater than the draw-down, whereas the converse results for the predominantly negative initial wave.

(ii) The maximum flow velocity occurs at the shoreline during the draw-down phase for the predominantly positive initial waves (cases a and c), whereas the

maximum velocity for the predominantly negative initial waves (cases b and d) occurs at the shoreline during the run-up. Since flow stresses are proportional to the square of velocity for turbulent flows, submerged objects, such as sediments, boulders, etc. tend to move shoreward when the initial waveform is a depression. On the other hand, they tend to move offshore when the initial wave is an elevation.

(iii) For the initial positive waveform, cases a and c, the maximum momentum flux (force) over the flow depth occurs after the maximum penetration, at the vicinity of the extreme draw-down location immediately before the flow reversal, hence the momentum flux is in the offshore direction. On the other hand, the maximum momentum flux occurs in the inshore direction prior to the maximum run-up penetration for cases b and d (the initial negative waveforms), and it occurs immediately after the flow reversal from the initial withdrawal caused by the leading depression wave. This indicates that the dominant momentum flux is shoreward for the predominantly negative initial waveform. Regardless of the initial waveform, the momentum flux, that is a measure of the net force exerted on a surface-piercing object over the depth, becomes maximum near the extreme draw-down location. This indicates that offshore structures placed close to the shore are vulnerable to tsunami attacks: for example, breakwaters, piers, LNG and oil loading terminals, ships moored offshore, etc.

(iv) The initial conditions of cases a and b have an identical initial waveform except the sign in the displacement, η . Although their run-up and run-down processes are different, their extreme values in velocity u and momentum flux f turn out to be identical. This is because the field of $\varphi(\sigma, \lambda)$ of case a is an exact mirror image of cases b as seen in (20) with $P(b) = 0$. Equation (10) further indicates that the fields of ψ and u in the (σ, λ) -space are also in the exact mirror images. However, the difference arises from the conversion of the (σ, λ) -space to the (x, t) -physical space by (4). Consequently, the extreme values of u and ψ are preserved in each case, although the location and the timing of the occurrence are different. Note that the parameter ψ represents the total mechanical energy. The linear-momentum flux (i.e. force) is computed by $f = qu^2 = \sigma^2 u^2$; hence, the magnitude of f is identical for cases a and b as well. It is emphasized that the mirror images in the extreme magnitudes of u, ψ , and f do not relate to the well-known equivalence in the maximum run-up penetration between the linear and nonlinear theories discussed by Carrier (1971) and Synolakis (1987). Instead, the linear-nonlinear correspondence in the maximum penetration results in the condition of $u = 0$ in (10). According to (20), the mirror correspondence in the extreme values of u and ψ and the identical value of f result even if $P(b) \neq 0$, as long as the initial conditions $F(b)$ and $P(b)$ of the two corresponding cases are identical in magnitude but have opposite signs. It is re-emphasized that even in such cases, the run-up/run-down processes in terms of the temporal and spatial patterns are different.

This work was supported by the US National Science Foundation (CMS-9907815, CMS-9978399) and the Department of Energy (DE-FG02-845R40158).

Appendix A. Derivation of (19)

$$\begin{aligned} \varphi(\sigma, \lambda) &= \int_0^\infty \rho J_0(\rho\sigma) \{ \bar{\varphi}(\rho, 0) \cos \rho\lambda/2 + (2/\rho) \bar{\varphi}_\lambda(\rho, 0) \sin \rho\lambda/2 \} d\rho \\ &= \int_0^\infty \rho J_0(\rho\sigma) \cos \rho\lambda/2 \int_0^\infty \sigma' J_0(\rho\sigma') P(\sigma') d\sigma' d\rho \\ &\quad + \int_0^\infty 2J_0(\rho\sigma) \sin \rho\lambda/2 \int_0^\infty \sigma' J_0(\rho\sigma') F(\sigma') d\sigma' d\rho \end{aligned}$$

$$\begin{aligned}
&= 2 \frac{\partial}{\partial \lambda} \int_0^\infty J_0(\rho\sigma) \sin \rho\lambda/2 \int_0^\infty \sigma' J_0(\rho\sigma') P(\sigma') d\sigma' d\rho \\
&\quad + 2 \int_0^\infty J_0(\rho\sigma) \sin \rho\lambda/2 \int_0^\infty \sigma' J_0(\rho\sigma') F(\sigma') d\sigma' d\rho \\
&= 2 \frac{\partial}{\partial \lambda} \int_0^\infty J_0(\rho\sigma) \sin \rho\lambda/2 \int_0^\infty \sigma' J_0(\rho\sigma') \int_0^\infty \delta(\sigma'' - \sigma') P(\sigma'') d\sigma'' d\sigma' d\rho \\
&\quad + 2 \int_0^\infty J_0(\rho\sigma) \sin \rho\lambda/2 \int_0^\infty \sigma' J_0(\rho\sigma') \int_0^\infty \delta(\sigma'' - \sigma') F(\sigma'') d\sigma'' d\sigma' d\rho \\
&= 2 \frac{\partial}{\partial \lambda} \int_0^\infty P(\sigma'') \left[\int_0^\infty J_0(\rho\sigma) \sin \rho\lambda/2 \int_0^\infty \sigma' J_0(\rho\sigma') \delta(\sigma'' - \sigma') d\sigma' d\rho \right] d\sigma'' \\
&\quad + 2 \int_0^\infty F(\sigma'') \left[\int_0^\infty J_0(\rho\sigma) \sin \rho\lambda/2 \int_0^\infty \sigma' J_0(\rho\sigma') \delta(\sigma'' - \sigma') d\sigma' d\rho \right] d\sigma'' \\
&= 2 \frac{\partial}{\partial \lambda} \int_0^\infty P(\sigma'') \left[\sigma'' \int_0^\infty J_0(\rho\sigma) \sin(\rho\lambda/2) J_0(\rho\sigma'') d\rho \right] d\sigma'' \\
&\quad + 2 \int_0^\infty F(\sigma'') \left[\sigma'' \int_0^\infty J_0(\rho\sigma) \sin(\rho\lambda/2) J_0(\rho\sigma'') d\rho \right] d\sigma'' \\
&= 2 \int_0^\infty P(b) G_\lambda(b, \sigma, \lambda) db + 2 \int_0^\infty F(b) G(b, \sigma, \lambda) db
\end{aligned}$$

where $G(b, \sigma, \lambda) = b \int_0^\infty J_0(\rho\sigma) \sin(\rho\lambda/2) J_0(\rho b) d\rho$.

Appendix B. Derivation of (22)

We wish to evaluate, explicitly and exactly, the following integral:

$$I(a, b, c) = \int_0^\infty J_0(at) J_0(bt) \sin ct dt. \quad (\text{B } 1)$$

Without loss of generality, we take a, b , and c to be real and non-negative.

Because of the symmetry in a - and b - exchange, it is sufficient to consider either $a \leq b$ or $a \geq b$, but not both. Using (9.1.20) in Abramowitz & Stegun (1964),

$$J_0(bt) = \frac{2}{\pi} \int_0^1 (1 - \zeta^2)^{-1/2} \cos(bt\zeta) d\zeta,$$

(B 1) can be expressed as

$$\begin{aligned}
I(a, b, c) &= \frac{2}{\pi} \int_0^1 d\zeta (1 - \zeta^2)^{-1/2} \int_0^\infty dt J_0(at) \cos(bt\zeta) \sin ct \\
&= \frac{1}{\pi} \int_0^1 d\zeta (1 - \zeta^2)^{-1/2} \int_0^\infty dt J_0(at) [\sin(c + b\zeta)t + \sin(c - b\zeta)t] \\
&= \frac{1}{\pi} \int_{-1}^1 d\zeta (1 - \zeta^2)^{-1/2} \int_0^\infty dt J_0(at) \sin(c - b\zeta)t.
\end{aligned}$$

The useful formula (6.671.7) in Gradshteyn & Ryzhik (1980) is

$$\int_0^\infty J_0(at) \sin \tau t dt = \begin{cases} 0 & \text{if } \tau < a, \\ (\tau^2 - a^2)^{-1/2} & \text{if } \tau > a. \end{cases} \quad (\text{B } 2)$$

In this formula, both a and τ are assumed to be positive. There is no loss of generality in taking $a > 0$; if τ is allowed to be negative, then (B 2) can be extended to

$$\int_0^\infty J_0(at) \sin \tau t \, dt = \begin{cases} -(\tau^2 - a^2)^{-1/2} & \text{for } \tau < -a, \\ 0 & \text{for } |\tau| < a, \\ (\tau^2 - a^2)^{-1/2} & \text{for } \tau > a, \end{cases}$$

or

$$\int_0^\infty J_0(at) \sin \tau t \, dt = (\tau^2 - a^2)^{-1/2} [\mathcal{H}(\tau - a) - \mathcal{H}(-\tau - a)],$$

where $\mathcal{H}(\bullet)$ is the heaviside function. The integral I can be now written as

$$I(a, b, c) = \frac{1}{\pi} \int_{-1}^1 d\zeta (1 - \zeta^2)^{-1/2} [(c - b\zeta)^2 - a^2]^{-1/2} [\mathcal{H}(c - b\zeta - a) - \mathcal{H}(-c + b\zeta - a)].$$

Observe that the argument of one of the Heaviside function vanishes, $c - b\zeta - a = 0$, when $\zeta = (c - a)/b$, and the other, $-c + b\zeta - a = 0$, when $\zeta = (-c - a)/b$. Also observe that at the integration limits of $\zeta = \pm 1$:

$$\begin{aligned} \zeta = \frac{c - a}{b} = -1 &\leftrightarrow c - a + b = 0, & \zeta = \frac{c - a}{b} = 1 &\leftrightarrow c - a - b = 0, \\ \zeta = \frac{-c - a}{b} = -1 &\leftrightarrow c + a - b = 0, & \zeta = \frac{-c - a}{b} = 1 &\leftrightarrow c + a + b = 0. \end{aligned}$$

It is therefore advantageous to take $a \geq b$ because $-c + b\zeta - a \leq -c + b - c \leq 0$ for $|\zeta| < 1$. Hence,

$$I(a, b, c) = \frac{1}{\pi} \int_{-1}^1 d\zeta (1 - \zeta^2)^{-1/2} [(c - b\zeta)^2 - a^2]^{-1/2} \mathcal{H}(c - b\zeta - a).$$

There are three cases to consider: (i) $c > a + b$, (ii) $a - b < c < a + b$, and (iii) $c < a - b$. In the case of $c > a + b$, $c - b\zeta - a > 0$ for $|\zeta| < 1$, therefore

$$I(a, b, c) = \frac{1}{\pi} \int_{-1}^1 d\zeta (1 - \zeta^2)^{-1/2} [(c - b\zeta)^2 - a^2]^{-1/2} \equiv \frac{1}{\pi b} \int_{-1}^1 d\zeta G(\zeta)^{-1/2}.$$

It can be observed that $G(\zeta) = 0$, when $\zeta = ((c + a)/b, (c - a)/b, 1, -1)$ in descending order. Noting the integration limits are $\zeta = \pm 1$, let

$$\sin^2 \phi = \frac{c + a - b}{2} \frac{\zeta + 1}{c + a - b\zeta}.$$

Then,

$$I(a, b, c) = \frac{2}{\pi \sqrt{c^2 - (a - b)^2}} K\left(\frac{4ab}{c^2 - (a - b)^2}\right), \quad (\text{B } 3)$$

where

$$K(k) = \int_0^{\pi/2} \frac{dv}{\sqrt{1 - k \sin^2 v}}$$

the complete elliptic integral of the first kind.

In the case of $a - b < c < a + b$, $c - b\zeta - a > 0$ when $\zeta < (c - a)/b$ which is between -1 and 1 .

$$I(a, b, c) = \frac{1}{\pi} \int_{-1}^{(c-a)/b} d\zeta (1 - \zeta^2)^{-1/2} [(c - b\zeta)^2 - a^2]^{-1/2} = \frac{1}{\pi b} \int_{-1}^{(c-a)/b} d\zeta G(\zeta)^{-1/2}$$

It can be observed that $G(\zeta) = 0$, when $\zeta = ((c + a)/b, 1, (c - a)/b, -1)$ in descending order, hence, let

$$\sin^2 \phi = \frac{2a}{c - a + b} \frac{b(\zeta + 1)}{c + a - b\zeta},$$

then, the integral becomes

$$I(a, b, c) = \frac{1}{\pi \sqrt{ab}} K\left(\frac{c^2 - (a - b)^2}{4ab}\right). \quad (\text{B } 4)$$

For the last case, $c < a - b$, then $c < a + b\zeta$ for $|\zeta| \leq 1$. Therefore

$$I(a, b, c) = 0. \quad (\text{B } 5)$$

In summary, for a, b and c all non-negative, (B 3)–(B 5) yield the explicit representation of the integral (B 1):

$$\begin{aligned} & \int_0^\infty J_0(at) J_0(bt) \sin ct \, dt \\ &= \begin{cases} \frac{2}{\pi \sqrt{c^2 - (a - b)^2}} K\left(\frac{4ab}{c^2 - (a - b)^2}\right) & \text{for } c > a + b \\ \frac{1}{\pi \sqrt{ab}} K\left(\frac{c^2 - (a - b)^2}{4ab}\right) & \text{for } |a - b| < c < a + b \\ 0 & \text{for } c < |a - b| \end{cases} \end{aligned}$$

REFERENCES

- ABRAMOWITZ, M. & STEGUN, I. A. 1964 *Handbook of Mathematical Functions with Formulas, Graphs, and Mathematical Tables*. National Bureau of Standards, Washington DC.
- CARRIER, G. F. 1971 The dynamics of tsunamis. In *Mathematical Problems in the Geophysical Sciences: 1. Geophysical Fluid Dynamics*. (ed. W. H. Reid), pp. 157–187. American Mathematical Society.
- CARRIER, G. F. & GREENSPAN, H. P. 1958 Water waves of finite amplitude on a sloping beach. *J. Fluid Mech.* **4**, 97–109.
- CARRIER, G. F. & NOISEUX, C. F. 1983 The reflection of obliquely incident tsunami. *J. Fluid Mech.* **133**, 147–160.
- GRADSHTEYN, I. S. & RYZHIK, I. M. 1980 *Table of Integrals, Series, and Products*. Academic.
- MAZOVA, R. KH. & PELINOVSKY, E. N. 1991 The increasing of tsunami runup height with negative leading wave. *Proc. IV Intl Symp. on Geophys. Hazards, Perugia, Italy*, p. 118.
- PELINOVSKY, E. N. & MAZOVA, R. KH. 1992 Exact analytical solutions of nonlinear problems of tsunami wave run-up on slopes with different profiles. *Natural Hazards* **6**, 227–249.
- SPIELVOGEL, L. Q. 1975 Single-wave run-up on sloping beaches. *J. Fluid Mech.* **74**, 685–694.
- SYNOLAKIS, C. E. 1987 The runup of solitary waves. *J. Fluid Mech.* **185**, 523–545.
- TADEPALLI, S. & SYNOLAKIS, C. E. 1994 The run-up of N-waves on sloping beaches. *Proc. R. Soc. Lond. A* **445**, 99–112.